Available online at www.sciencedirect.com
ScienceDirect
Geochimica et Cosmochimica Acta 73 (2009) 696–711
Geochimica et Cosmochimica Acta
www.elsevier.com/locate/gca

Iron biomineralization by anaerobic neutrophilic iron-oxidizing bacteria

Jennyfer Miot [a,*], Karim Benzerara [a], Guillaume Morin [a], Andreas Kappler [b], Sylvain Bernard [c], Martin Obst [d], Céline Férard [a], Fériel Skouri-Panet [a], Jean-Michel Guigner [a], Nicole Posth [b], Matthieu Galvez [a], Gordon E. Brown Jr. [e,f], François Guyot [a]

[a] *Institut de Minéralogie et de Physique des Milieux Condensés, UMR 7590, CNRS, Universités Paris 6 et Paris 7, et IPGP, 140, rue de Lourmel, 75 015 Paris, France*
[b] *Geomicrobiology Center for Applied Geoscience (ZAG), University of Tuebingen, Sigwartstrasse 10, 72076 Tuebingen, Germany*
[c] *Laboratoire de Géologie, Ecole normale supérieure, CNRS, 24 rue Lhomond, 75005 Paris, France*
[d] *BIMR McMaster University Hamilton & Canadian Light Source, 101 Perimeter Road, Saskatoon, Sask., Canada S7N OX4*
[e] *Surface & Aqueous Geochemistry Group, Department of Geological & Environmental Sciences, Stanford University, Stanford, CA 94305-2115, USA*
[f] *Stanford Synchrotron Radiation Laboratory, SLAC, Menlo Park, CA 94025, USA*

Received 2 June 2008; accepted in revised form 21 October 2008; available online 11 November 2008

Abstract

Minerals formed by bio-oxidation of ferrous iron (Fe(II)) at neutral pH, their association with bacterial ultrastructures as well as their impact on the metabolism of iron-oxidizing bacteria remain poorly understood. Here, we investigated iron biomineralization by the anaerobic nitrate-dependent iron-oxidizing bacterium *Acidovorax* sp. strain BoFeN1 in the presence of dissolved Fe(II) using electron microscopy and Scanning Transmission X-ray Microscopy (STXM). All detected minerals consisted mainly of amorphous iron phosphates, but based on their morphology and localization, three types of precipitates could be discriminated: (1) mineralized filaments at distance from the cells, (2) globules of 100 ± 25 nm in diameter, at the cell surface and (3) a 40-nm thick mineralized layer within the periplasm. All of those phases were shown to be intimately associated with organic molecules. Periplasmic encrustation was accompanied by an accumulation of protein moieties. In the same way, exopolysaccharides were associated with the extracellular mineralized filaments. The evolution of cell encrustation was followed by TEM over the time course of a culture: cell encrustation proceeded progressively, with rapid precipitation in the periplasm (in a few tens of minutes), followed by the formation of surface-bound globules. Moreover, we frequently observed an asymmetric mineral thickening at the cell poles. In parallel, the evolution of iron oxidation was quantified by STXM: iron both contained in the bacteria and in the extracellular precipitates reached complete oxidation within 6 days. While a progressive oxidation of Fe in the bacteria and in the medium could be observed, spatial redox (oxido-reduction state) heterogeneities were detected at the cell poles and in the extracellular precipitates after 1 day. All these findings provide new information to further the understanding of molecular processes involved in iron biomineralization by anaerobic iron-oxidizing bacteria and offer potential signatures of those metabolisms that can be looked for in the geological record.

1. INTRODUCTION

Iron-oxidizing bacteria and archeae may have a significant impact on the Earth's surface geochemistry, by taking part in the redox cycling of iron under both oxic and anoxic

* Corresponding author. Fax: +33 144273785.
E-mail address: miot@impmc.jussieu.fr (J. Miot).

0016-7037/$ - see front matter © 2008 Elsevier Ltd. All rights reserved.
doi:10.1016/j.gca.2008.10.033

conditions (e.g. Ghiorse, 1984; Konhauser, 1998; Fortin and Langley, 2005; Kappler and Straub, 2005; Weber et al., 2006). Various micro-organisms can retrieve energy from the aerobic oxidation of Fe(II) in oxic environments at acidic (Lazaroff et al., 1985; Clarke et al., 1997; Kozubal et al., 2008) or neutral pH (Hallberg and Ferris, 2004). Over the last 15 years, the discovery of bacteria capable of using Fe(II) as an electron donor under anoxic conditions and at neutral pH has boosted interest in the study of these metabolisms. Among them, two are potentially widespread in neutral-pH anoxic habitats (for instance in river sediments, lakes or deep-sea environments): (1) anoxygenic photosynthesis using Fe(II) as an electron donor (Widdel et al., 1993; Ehrenreich and Widdel, 1994; Heising and Schink, 1998) and (2) iron oxidation coupled to nitrate reduction (Hafenbradl et al., 1996; Straub et al., 1996; Benz et al., 1998; Straub and Buchholz-Cleven, 1998; Kappler et al., 2005a).

Fe(II) oxidation driven by iron-oxidizing nitrate-reducing bacteria leads to the formation of Fe(III) compounds. The chemistry and mineralogy of these Fe(III) compounds depend on environmental conditions. Eq. (1) summarizes this reaction with formation of Fe(III) hydroxides:

$$2Fe^{2+} + 5H_2O + NO_3^- = 2Fe(OH)_3 + 4H^+ + NO_2^- \quad (1)$$

Due to their low solubility at neutral pH (Cornell and Schwertmann, 2003), the Fe(III) by-products of this reaction, represented here by iron hydroxides, precipitate rapidly in the direct vicinity of the cells. However, the accurate localization of iron biominerals with respect to the cellular ultrastructures remains unclear. Recent studies tend to indicate that different strains (utilizing different metabolisms) exhibit different biomineralization patterns. For instance, the nitrate-reducing iron-oxidizing β-proteobacterial strain BoFeN1 (Kappler et al., 2005a) becomes encrusted with Fe(III) minerals as iron oxidation proceeds, whereas the photosynthetic iron-oxidizing purple bacterium *Rhodobacter ferroxidans* strain SW2 (Ehrenreich and Widdel, 1994) does not encrust, even after complete oxidation of Fe(II) (Kappler and Newman, 2004). It has been suggested that this is related to a differential adaptation to iron oxidation, yet the mechanisms accounting for these two distinct phenotypes are still poorly understood. A precise characterization and localization of iron-containing minerals associated with the cells is thus needed to better constrain these mechanisms. This in turn might offer useful signatures for the search of the by-products of such metabolisms in the geological record (e.g. Konhauser, 1998; Little et al., 2004).

In this study, we chose to focus on the iron-oxidizing nitrate-dependent strain BoFeN1, phylogenetically close to the β-proteobacterium *Acidovorax* sp. We used several microscopic and spectroscopic techniques, in particular Transmission Electron Microscopy (TEM), X-ray Absorption Spectroscopy (XANES: X-ray Absorption Near-Edge Spectroscopy and EXAFS: Extended X-ray Absorption Fine Structure) and Scanning Transmission X-ray Microscopy (STXM) to characterize the cell-mineral associations in batch cultures of BoFeN1. The evolution of iron redox state and the association of organics with iron minerals are documented at the submicrometer scale over the time course of a culture.

2. MATERIALS AND METHODS

2.1. Bacterial strain and growth conditions

The nitrate-dependent Fe(II)-oxidizing strain BoFeN1, isolated from Lake Constance littoral sediments (Kappler et al., 2005a), was cultivated in freshwater mineral medium prepared after Ehrenreich and Widdel (1994). Phosphate was provided as KH_2PO_4 at an initial concentration of 4.3 mM. The bacteria were cultured in this medium complemented with 5 mM acetate (provided as sodium acetate) and 10 mM nitrate (provided as sodium nitrate) in the presence or absence of Fe(II) (provided as $FeCl_2$). Although BoFeN1 clearly oxidizes metabolically Fe(II), it should be noted that it has not been demonstrated yet that BoFeN1 cells can use Fe as an energy source (Kappler et al., 2005a). The addition of Fe(II) at a total concentration of 10 mM led to the precipitation of a whitish phase (consisting of Fe(II)-phosphate, mostly vivianite $Fe_3(PO_4)_2$), which was subsequently removed by filtration through 0.22 μm Millipore filters, in an anoxic glove-box ($p(O_2) < 50$ ppm). After filtration, the medium contained 5.4 mM dissolved Fe(II) and 1.3 mM phosphate. For each culture, 25 mL of medium were transferred into a 58 mL serum bottle that was flushed with N_2/CO_2 (80/20%), closed with a butyl rubber stopper and crimped. BoFeN1 was inoculated (10%) from an acetate–nitrate–grown culture (culture without iron). Cultures were incubated at 30 °C. For TEM and STXM analyses, samples of the same culture were taken in an O_2-free glove-box at several subsequent time steps.

2.2. Analytical methods

Growth was followed by measuring the total soluble protein content using the Bradford assay. One microliters of culture was mixed with a solution of oxalic acid (pH 3, 0.2 M) in order to dissolve iron-bearing minerals and with 6.1 M trichloroacetic acid to precipitate proteins. After centrifugation (11000*g*, 30 min) and removal of the supernatant, proteins were dissolved in 0.1 M NaOH at 60 °C for 6 min. The absorbance of the samples was measured at 595 nm after reaction with the Bradford reagent (BioRad, microassay). Experiments were conducted in duplicate.

In order to analyze dissolved iron, 200 μL of a culture suspension were sampled with a syringe and filtered through 0.22 μm Millipore filter in an anoxic glove-box. The dissolved Fe(II) content of the filtrate was determined by the ferrozine assay (Viollier et al., 2000) after dilution in 1 M HCl.

2.3. Synthesis of model compounds

To determine the Fe redox state of the samples by STXM at the Fe $L_{2,3}$-edges, we used pure Fe(II)- and Fe(III)-phosphates as reference compounds. Both have been synthesized under anoxic conditions. Fe(II)-phosphate was obtained by addition of 10 mM Fe(II) (as $FeCl_2$), 5 mM acetate and 10 mM nitrate in the growth medium, which led to the precipitation of a whitish Fe(II)-phosphate phase. Fe(III)-phosphate was obtained by the addition of

10 mM Fe(III) (as $FeCl_3$), 5 mM acetate and 10 mM nitrate in the growth medium. Both precipitates were rinsed twice with degassed distilled water and dried under vacuum inside an anoxic glove-box. As shown by XRD, this Fe(II)-phosphate phase consisted of vivianite, whereas the Fe(III)-phosphate was amorphous (Fig. 2). Based on TEM, XRD and XAS analyses, these model compounds likely represented the closest analogues of the phases formed in the BoFeN1 cultures. Therefore, we used experimental Fe $L_{2,3}$-edge spectra of these model compounds to analyze iron oxidation state of BoFeN1 in STXM experiments, instead of goethite, hematite, or siderite. XAS data of the BoFeN1 samples were least-square fitted using linear combinations of these two model compounds and of a 2-line ferrihydrite (Fh2L) synthesized following the procedure by Schwertmann and Cornell (1991).

2.4. Mineral characterization by X-ray diffraction

The bulk mineralogical composition was determined by X-ray diffraction (XRD) measurement performed on the solid phase collected from a 13-day old culture compared to Fe(II)- and Fe(III)-phosphate model compounds. Samples were prepared under anoxic conditions in an anoxic glove-box. The culture was centrifuged (5000*g*, 10 min). The solid phase was rinsed twice using degassed distilled water and vacuum-dried. The powder was grinded in an agate mortar and dispensed in a borosilicate capillary, that was sealed with glue before analysis in the diffractometer. This preparation guaranteed strictly anoxic conditions for XRD analyses. XRD measurements were performed with Co$K\alpha$ radiation on a Panalytical® X'Pert Pro MPD diffractometer mounted in Debye–Scherrer configuration using an elliptical mirror to obtain a high flux parallel incident beam and an X'Celerator® detector to collect the diffracted beam. Data were recorded in the continuous-scan mode within the 5–80° 2θ range with a step of 0.03°, and a counting time of 12–24 h per sample.

2.5. XAS analyses

2.5.1. XAS data collection

In order to limit Fe(II) oxidation under the X-ray beam and to enhance EXAFS signal on our nano-sized and poorly ordered mineral phases, all data were recorded at 10–15 K using a modified Oxford® liquid He cryostat. Samples were transferred from the glove-box into a liquid nitrogen bath and then into the cryostat, where they were placed under He atmosphere. This procedure preserved anoxic conditions during sample transfer and analysis. EXAFS data on all samples except the Fe(II)-phosphate and Fh2L, were recorded at the Fe K-edge, using a Si(2 2 0) double-crystal monochromator on beamline 10–2 at the Stanford Synchrotron Radiation Laboratory (SSRL). Monochromator was detuned 50% in order to reject harmonics. Data on the final product of Fe(II) bio-oxidation by BoFeN1 were collected in fluorescence detection mode using a 13-element Ge-array detector and a 3 $\Delta\mu$ Mn filter to attenuate elastic scattering. For EXAFS data collection, energy resolution was around 1 eV, with a beam size of $2 \times 3\ mm^2$ achieved by vertical and horizontal focusing, with a Pt coated elliptic mirror. For XANES data collection, resolution was improved using vertical slits of 0.25 mm height from ~1.5 to ~0.5 eV. Data on the Fe(III)-phosphate model compounds were recorded in transmission mode with an unfocused beam collimated by $2 \times 3.5\ mm^2$ slits, which explain XANES data for this sample are not as well-resolved as for other samples studied. Four EXAFS scans were accumulated for each sample in order to obtain a reliable signal-to-noise ratio up to $k = 11\ Å^{-1}$. No measurable change in iron oxidation state was observed during beam exposure under these experimental conditions. XAS data of the Fe(II)-phosphate model compound were recorded in transmission at 10 K on the SAMBA beamline at the SOLEIL (Source Optimisée de Lumière d'Énergie Intermédiaire du LURE) synchrotron using a dynamical sagittal-focusing Si(1 1 1) monochromator. EXAFS data on the Fh2L were recorded at 10 K on the D44 beamline at the Laboratoire pour l'Utilisation du Rayonnement Electromagnétique (LURE) using a Si(1 1 1) double-crystals monochromator. XANES data on this sample were recorded in transmission mode at 10 K on the BM29 ESRF (European Synchrotron Radiation Facility) beamline using a Si(1 1 1) double-crystals monochromator. For all experiments, energy was calibrated by using a double-transmission setup; the first inflection point of the Fe metal foil K-edge was set at 7111.1 eV (Wilke et al., 2001).

2.5.2. XAS data analysis

X-ray absorption spectra were averaged using the SixPack software (Webb, 2004). EXAFS data were extracted using the XAFS program (Winterer, 1997) following the procedure detailed previously by Morin et al. (2008). Radial distribution functions around the Fe absorber were obtained by calculating the Fourier transform (FT) of the $k^3\chi(k)$ EXAFS functions using a Kaiser–Bessel window within the 2.7–11 $Å^{-1}$ k-range with a Bessel weight of 2.5. Least-squares fitting of the unfiltered EXAFS functions were performed with the plane-wave formalism, using a Levenberg–Marquard minimization algorithm. Ab initio phase shifts and total amplitude functions employed in this fitting procedure were calculated with the curved-wave formalism using the ab initio FEFF 8 code (Ankudinov et al., 1998) and the atomic positions from the crystal structure of goethite (Forsyth et al., 1968) and vivianite (Fejdi et al., 1980). The fit quality was estimated within the 2.7–11 $Å^{-1}$ k-range, using a reduced χ^2 of the following form:

$$\chi^2 = N_{ind}/(N_{ind} - p) \sum \left(k^4\chi(k)_{exp} - k^4\chi(k)_{calc}\right)^2 \quad (2)$$

with N_{ind} (the number of independent parameters) $= (2\Delta k \Delta R)/\pi$, p is the number of free fit parameters. The fitting procedure was performed on k^4-weighted $\chi(k)$ functions in order to emphasize the signal at high k values, which improves the accuracy of the fitted distances for light backscattering atoms. Data are however displayed as k^3-weighted $\chi(k)$ functions. The $\chi(k)$ function of the BoFeN1 sample was also fit within the 3–10.5 $Å^{-1}$ k-range by linear least-squares fitting (LSF), using linear combinations of

$k^3\chi(k)$ spectra of the Fh2L and Fe(III)-phosphate model compounds.

2.6. Microscopic analyses

Two types of samples were prepared for TEM analyses. First, ultrathin sections were prepared by ultramicrotomy. Cells were fixed for 2 h in 1% glutaraldehyde at 4 °C, centrifuged (5000*g*), rinsed three times in 0.1 N sodium cacodylate buffer (pH 7.2) for 18 h at 4 °C. They were then post-fixed for 90 min in 1% OsO_4 in the same buffer, rinsed three times in distilled water, dehydrated in graded ethanol and propylene oxide-1,2 and progressively embedded in epoxy resin (Epoxy, Fluka Chemika). Ultrathin sections (70-nm thick) were cut with a LEICA ultramicrotome (EM-UC6). After deposition on copper grids, they were stained with uranyl acetate (2% w/v) and lead citrate (2 g L^{-1}). The whole preparation was conducted in air, since fixation with glutaraldehyde requires O_2. As a consequence, TEM observations could not allow the determination of the redox state of iron, which was determined by STXM analyses (see infra).

For Scanning Transmission Electron Microscopy (STEM), High-Resolution TEM (HRTEM), tomography observations and Energy Dispersive X-ray Spectroscopy (XEDS) measurements, whole cells were deposited on a carbon-coated 200-mesh copper grid after two rinses in degassed distilled water and dried in an anoxic glove-box. STEM and HRTEM observations, as well as XEDS analyses were performed with a JEOL2100 Microscope operating at 200 kV. STEM observations were performed in dark field (DF) mode. XEDS maps were acquired in STEM DF mode, with a focused electron beam (1 nm). Selected area electron diffraction (SAED) patterns were obtained on areas of interest. Tomography was performed using a JEOL2100 TEM, equipped with a LaB_6 source, operating at 200 kV. Samples were tilted between −60° and +50°, and images were acquired with Digital-Micrograph at 1° steps.

2.7. Scanning Transmission X-ray Microscopy

2.7.1. Sample preparation

Preliminary STXM experiments showed that the samples are highly sensitive to oxidation by O_2. We thus developed a specific protocol to keep the samples under an anoxic atmosphere from preparation to transfer into the microscope. Tests on the reference highly O_2-sensitive Fe(II)-phosphate showed that this protocol was efficient in preserving the sample from any oxidation detectable by XANES. The entire preparation was performed in an anoxic glove-box. One microliters of a suspension of BoFeN1 culture (or of reference compounds) was sampled at different stages of each culture (3 h to 6 days). Each sample was rinsed twice in degassed distilled water. The volume (0.3 μL) of each sample was then deposited on a silicon nitride membrane (Norcada Inc., Canada) fixed on an aluminium sample holder and allowed to dry at ambient temperature. A second silicon nitride membrane was then deposited in contact with the first one and sealed with araldite. Sample holders were stored in sealed aluminized paper (Protpack, UK) before transfer to the synchrotron. The sealed pockets were opened under a nitrogen flow just before placing the sample inside the microscope, in which air had been replaced by nitrogen. After sample transfer, nitrogen was replaced by helium at 1 atm.

2.7.2. STXM experiments

Some of the STXM observations at the Fe $L_{2,3}$-edges were performed at the Swiss Light Source (SLS, Villigen) at the PolluX beamline. Some of the observations at the Fe $L_{2,3}$-edges and all the observations at the C K-edge were performed at the spectromicroscopy beamline 10ID-1 at the Canadian Light Source (CLS, Saskatoon). Additional information on the PolluX beamline can be found in Bernard et al. (2007). The beamline 10ID-1 at the CLS was described in detail by Kaznatcheev (2007). Both beamlines have an energy resolving power $E/\Delta E > 3000$. The energy scales for this study were calibrated using the well-resolved 3p Rydberg peak of gaseous CO_2 for the C K-edge and the major peak of hematite at 708.7 eV for the Fe L_3-edge.

2.7.3. Data processing

Image stacks were acquired at the C K-edge and at the Fe $L_{2,3}$-edges. They were performed by scanning the sample in the *x*–*y* direction at each energy increment over the energy range of interest. Potential sample damages caused by the incident photon beam (i.e. changes of the Fe redox state) were quantified by monitoring spectral changes at the Fe $L_{2,3}$-edge with increasing dwell times up to several tens of milliseconds (Fig. EA-1). However, no significant changes were observed for typical dwell times used during analyses of the samples (i.e. around 0.8 ms per energy- and image-point). The aXis2000 software-package (Hitchcock, 2001) was used for processing image stacks and XANES spectra. Images were recorded on transmission scale and converted into optical density (OD) according to the following equation:

$$\mathrm{OD} = -\ln(I/I_0) \tag{3}$$

wherein I represents the measured intensity at the point of interest and I_0 represents the intensity outside the sample that includes the absorption by silicon nitride windows. Qualitative speciation maps were obtained by subtracting OD-images obtained at an energy below the absorption edge from OD-images taken at the energies of specific absorption peaks.

Quantitative Fe-speciation maps were calculated from the image stacks by singular value decomposition using the stack-fit routine in aXis2000. The algorithm fits the spectra of each individual pixel with a linear combination of the two normalized reference spectra (Fe(II)- and Fe(III)-phosphate model compounds) plus a constant, accounting for the absorption background. Composite maps were obtained by overlaying on the same image the Fe(II) (blue) and the Fe(III) (red) maps using a common intensity scale for both color channels.

XANES spectra were extracted from the stacks on regions of interest. For C K-edge spectra, the edge jump was normalized to 1. For Fe $L_{2,3}$-edges spectra, we normal-

ized the area below the L_2 and L_3-edges to 1 and multiplied the absorbance of the compounds containing mainly Fe(II) (major peak at 707 eV) by a 4/5 correction factor to take into account the difference in the occupancy of the 3d orbitals in Fe^{2+} and Fe^{3+} ions, neglecting the variation of radial integrals (Thole et al., 1994). We fit the normalized spectra with linear combinations of the normalized reference spectra of the Fe(II)- and Fe(III)-phosphate model compounds, applying the CGO (Conjugate Gradient Optimization method) curve fit routine in aXis2000. Fit results allowed estimating the Fe(III)/Fe(total) content of regions of interest. Standard deviations (SD) were calculated from the deviation between the fit and the data and were systematically less than 1%. Additionally, we performed duplicates (two independent cultures and analyses) for the 1- and 3-day old samples, that indicated a good reproducibility of the Fe(III)/Fe(total) ratio estimations, with a standard deviation lower than 10%.

3. RESULTS

3.1. Bacterial growth and Fe oxidation by-products formed in BoFeN1 cultures

Bulk measurements on the cultures showed that starting from 4 to 6 mM of dissolved Fe(II), iron was completely oxidized within 3 days, which coincided with the start of the stationary phase of growth (Fig. 1). In contrast, no significant Fe(II) oxidation was observed in non-inoculated samples over the duration of the experiment.

In the cultures, the oxidation of Fe(II) could be observed macroscopically by the appearance of an orange precipitate. The solid phase, collected after 13 days of culture, was XRD-amorphous (Fig. 2) and was therefore further characterized by XAS (Table 1, Figs. 3 and EA-2). The position of the pre-edge of the BoFeN1 sample at 7113.7 eV

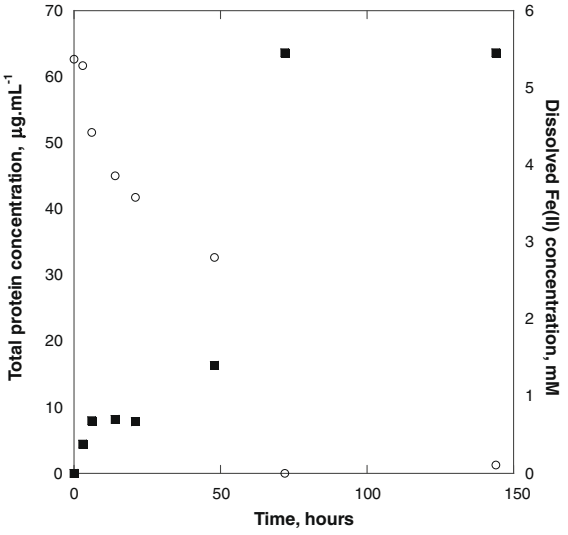

Fig. 1. Growth curve of BoFeN1 and Fe(II) consumption in the presence of acetate (5 mM), nitrate (10 mM) and ferrous iron over a period of 6 days. (■): total protein concentration, (○): dissolved Fe(II) concentration.

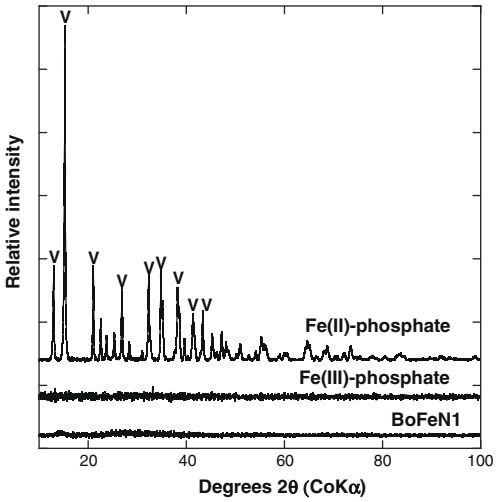

Fig. 2. X-ray diffractograms of precipitates collected from BoFeN1 cultures after 13 days and of reference Fe(II)- and Fe(III)-phosphate.

indicated that iron was mostly present as Fe(III) in the end-product of iron bio-oxidation by BoFeN1 after 13 days of culture (Fig. 3, Wilke et al., 2001), which is consistent with the shift of 2 eV in the absorption maximum of the XANES spectrum compared to the Fe(II)-phosphate model compound. Additionally, the shape of the pre-edge peak is consistent with a dominant octahedral coordination of Fe(III) in this mineral. Best fits of the EXAFS data of this sample and of the model compounds ferrihydrite,

Table 1
Fitting results for Fe K-edge EXAFS data of 13-day old BoFeN1 cultures and of the 2-line ferrihydrite, Fe(II)- and Fe(III)-phosphate model compounds. Coordination number (N), interatomic distance (R), Debye–Waller parameter (σ) and energy offset (E_0). Fit quality was estimated by a reduced χ^2 parameter (see text). The low coordination number for Fe–O pairs ($N = 3.5$–4.5) is attributed to cancellations due to strong distortions of the Fe(O, OH, H_2O) octahedra (see e.g. Michel et al., 2007 for details on ferrihydrite structure).

Sample	N (±0.3)	Bond	R (Å) (±0.05)	σ (Å) (±0.02)	E_0 (eV) (±3)	χ^2
2-Line ferrihydrite	4.2	Fe—O	1.96	0.11	1	9.68
	1.4	Fe—Fe	3.03	0.10		
	2.6	Fe—Fe	3.44	0.10		
Fe(II)-phosphate	4.0	Fe—O	2.09	0.09	4	37.1
	1.8	Fe—P	3.29			
	0.9	Fe—Fe	3.00			
	2.6	Fe—Fe	4.71			
Fe(III)-phosphate	3.5	Fe—O	1.98	0.07	3	19.9
	2.5	Fe—P	3.23	0.11		
BoFeN1	4.5	Fe—O	1.97	0.10	1	10.7
	1.3	Fe—P	3.19	0.05		
	0.3	Fe—Fe	3.52	0.05		

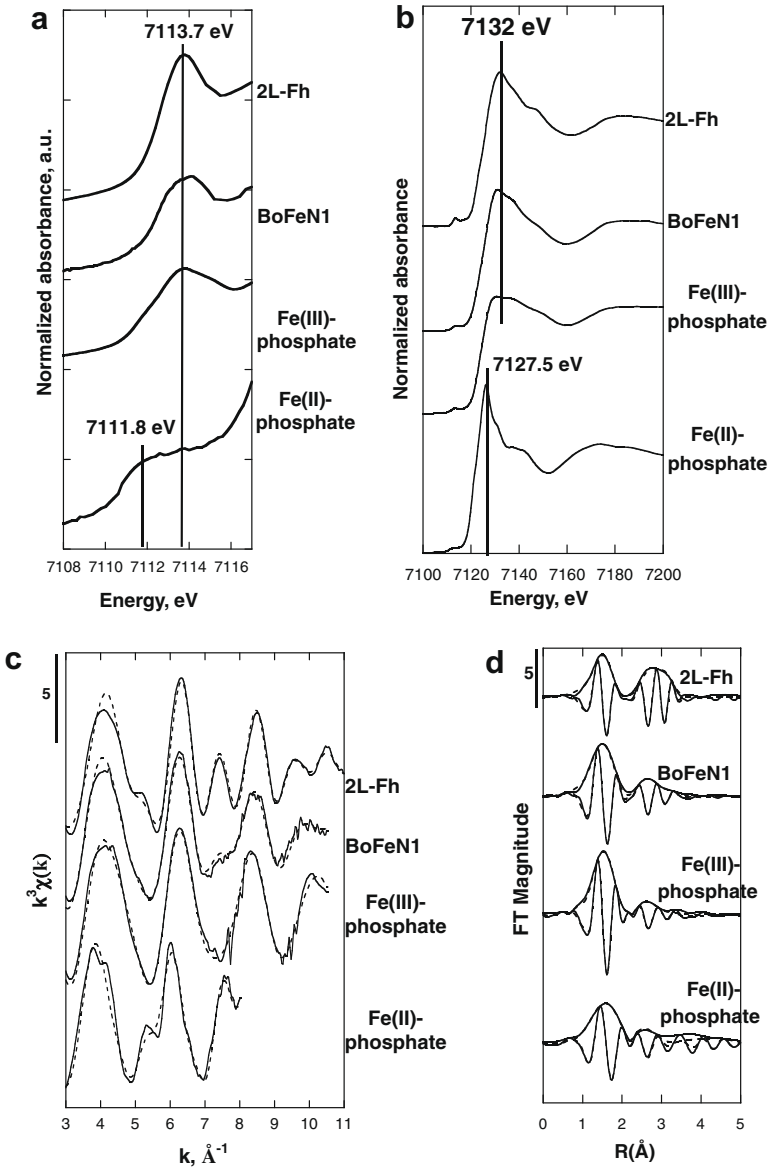

Fig. 3. X-ray absorption spectroscopy measurements on the bulk cultures of BoFeN1 after 13 days. (a) XANES spectra at the Fe Kα-edge of 13-day old BoFeN1 cultures and of 2L-ferrihydrite (Fh2L), Fe(III)- and Fe(II)-phosphate model compounds. (b) Unfiltered $k^3\chi(k)$ data compared with the spectra of the model compounds 2-line ferrihydrite (Fh2L), Fe(II)- and Fe(III)-phosphate. (c) Corresponding Fourier transforms. Solid lines show the data and dashed lines the best fits of the $k^3\chi(k)$ data (see Table 1).

Fe(II)-, and Fe(III)-phosphates are listed in Table 1 and plotted in Fig. 3. The first- and second-neighbour shells in EXAFS data of the 13-day old BoFeN1 culture consisted of oxygen, phosphate and iron ligands at 1.97 ± 0.05, 3.19 ± 0.05 and 3.52 ± 0.05 Å, respectively. These distances are consistent with those measured on the reference amorphous Fe(III)-phosphate (Table 1), i.e. FeO_6 octahedra sharing corners with PO_4 tetrahedra (Rose et al., 1996, 1997). The structure of this phase could thus be close to the structure of iron arsenate recently proposed by Paktunc et al. (2008). The absence of Fe–Fe pairs at a distance of 3.0–3.2 Å, corresponding to edge-sharing FeO_6 octahedra that are the structural basis of all iron oxyhydroxides, rules out the possibility this phase would be an iron oxyhydroxide with adsorbed phosphate. In contrast, our EXAFS results clearly indicate that the final Fe-oxidation product in BoFeN1 cultures consists of a mixed Fe–PO_4 (oxy)hydroxide. Additionally, a linear decomposition of the $k^3\chi(k)$ function of the BoFeN1 sample with the $k^3\chi(k)$ functions of Fh2L and of the amorphous Fe(III)-phosphate model compound (Fig. EA-2) was performed. Although previous results clearly indicate that the iron minerals are not composed of ferrihydrite, this decomposition allowed the local order of the iron minerals formed in BoFeN1 cultures to be investigated. These results indicate that the local structure of the minerals formed in BoFeN1 cultures is more ordered than the local structure of the reference amorphous Fe(III)-phosphate, but remains very close to.

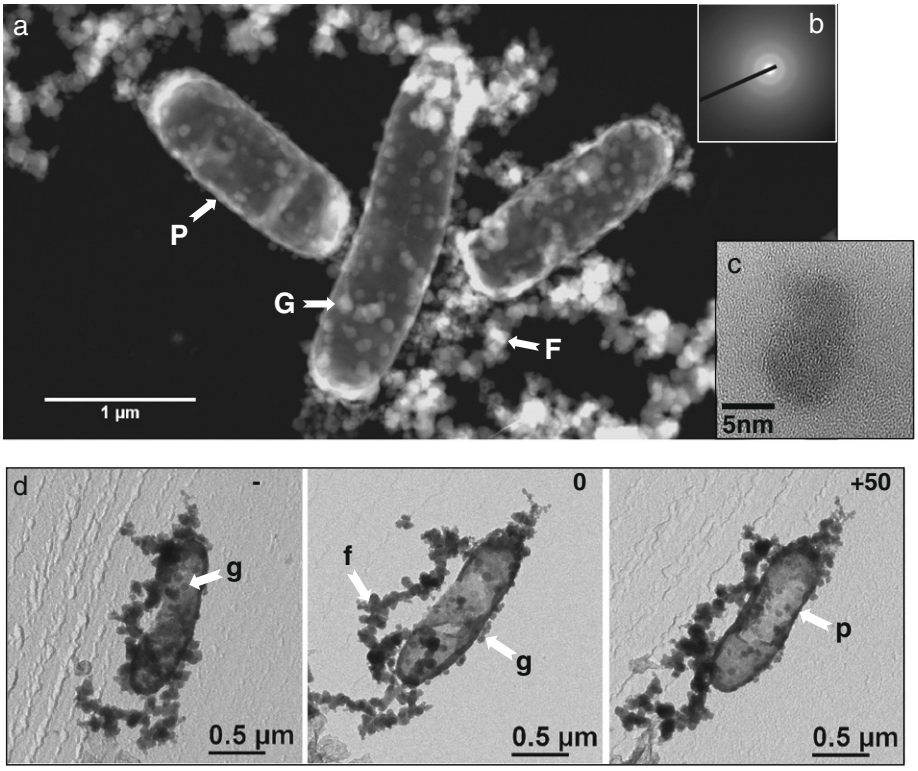

Fig. 4. TEM and STEM observation of Fe-precipitates in BoFeN1 cultures. (a) STEM image (dark field) showing three cells and Fe-containing precipitates (bright areas). Three types of precipitates can be observed (white arrows): mineralized filaments (F), globules at the cell surface (G) and periplasmic encrustation (P) are pointed by white arrows. (b) Electron diffraction pattern obtained on a globule at the cell surface and showing diffuse rings indicating that the globules are amorphous. (c) High-resolution image of a single particle on a filament, showing that it is amorphous. (d) TEM tilt series (−60°, 0° and +50°, movie available as Supporting Information EA-3) of an encrusted cell and mineralized filaments.

Indeed, a component having a local structure similar to Fh2L is more expressed in the BoFeN1 sample than in the reference Fe(III)-phosphate. All these results are consistent with the production of amorphous Fe(III)-phosphates in BoFeN1 cultures. This phase exhibits similarities in its EXAFS signal with the natural oxidation product of vivianite, i.e. santabarbaraite (Pratesi et al., 2003) but determining the exact nature of this mineral would need further investigations.

3.2. Microscopic characterization of the precipitates formed in BoFeN1 cultures

The minerals formed in BoFeN1 cultures were further characterized by a set of microscopic methods. As illustrated in Fig. 4, three different types of precipitates could be discriminated, based on their morphology and localization with respect to the cells. (1) Mineralized filaments formed by assemblies of 95 ± 30 nm in diameter spherules were observed outside the cells, and usually in the vicinity of the cells. (2) 100 ± 25 nm in diameter globules covered the cell surface (Fig. 4a and c). The extracellular localization of these globules, in contact with the cell outer membrane was confirmed by tomography performed on mineralized bacteria (Fig. 4d and Movie EA3). (3) An electron dense layer outlining the cell surface was observed both by STEM in dark field mode (Fig. 4a) and by TEM (Fig. 4d). As shown by tomography on whole cells, this layer remained visible whatever the tilt angle (from −60° to +50°, Fig. 4d and Movie EA3). TEM observations of stained thin sections unambiguously indicated that this mineral layer was located within the periplasm, in between the cytoplasmic and the outer membranes (Fig. 5a and b). This is consistent with the observation of a rather constant thickness (40 nm) of this electron dense layer observed by STEM in dark field mode on samples of whole bacteria (Fig. 5c and d). In the following, we refer to the formation of this mineral layer in the periplasm as "cell encrustation". This mineralization almost systematically displayed an asymmetric pattern at the cell poles: one pole was heavily mineralized with thicknesses up to 350 nm, whereas the dense layer on the opposite pole did not exceed 40 nm in thickness (Fig. 5c). Consistently with XRD and XAS analyses, all three types of precipitates were amorphous by electron diffraction (Fig. 5b and c) and composed of Fe, P and O (Fig. 6).

Detection and mapping of organic molecules were performed using STXM at the C K-edge (Fig. 7). Different biochemical compounds can be discriminated at this edge based on their XANES spectra, in particular the energy position of their maximum absorption peaks (e.g. Benzerara et al., 2004a). Fig. 7b–d show the maps

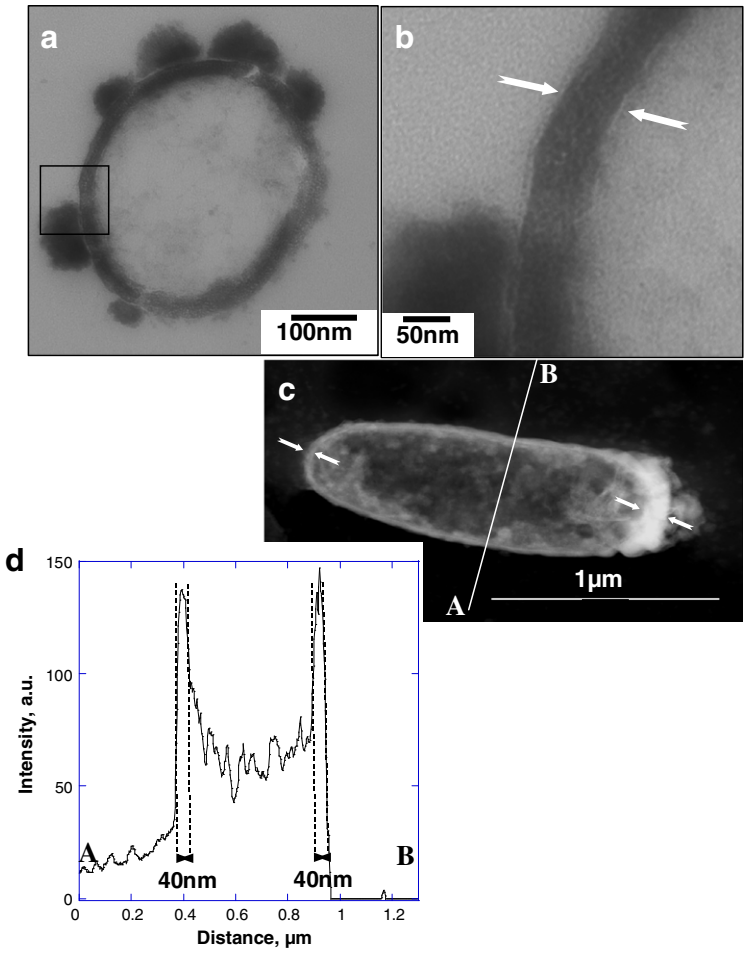

Fig. 5. TEM study of periplasmic encrustation within BoFeN1 cells after 6 days of culture. (a) TEM bright-field image of a transversal section of a BoFeN1 cell stained with U-acetate and Pb-citrate. (b) TEM bright-field image of a detail of the BoFeN1 cell wall shown in (a). White arrows point the outer and inner membranes enclosing the precipitates. (c) STEM image (dark field) of an encrusted cell. Bright areas are enriched in iron. White arrows point the asymmetric mineral thickening at the poles, with the right pole being thicker than the left pole. (d) Intensity profile taken along the A–B line indicated from panel (c), evidencing the 40-nm thick encrustation within the periplasm. Such measurements can be processed all around the cells and show the relatively constant thickness (except at one of the poles) of this encrustation consistent with the width of the periplasm.

of proteins (—(C=O)—(NH)—, 288.2–280 eV), polysaccharides (289.2–280 eV) and iron (708–700 eV), respectively, on the same area. The periplasmic iron-rich layer contained high amounts of organic carbon. XANES spectra obtained on the periplasm of many cells were similar to whole bacteria XANES spectra (Fig. 7e) and contained mostly amide functional groups characteristic of proteins. In addition, different organic molecules were observed in association with extracellular iron minerals (Fig. 7c and d). C K-edge XANES spectra recorded on these phases exhibited major peaks at 288.6 and 289.9 eV and were similar to XANES spectra of reference polysaccharides (Fig. 7e).

3.3. Spatial and temporal variations of cell encrustation among a bacterial population

Aliquots of BoFeN1 cultures were sampled for STEM analysis 30 min, 3 h, 6 h, 1 day, 3 days and 6 days after inoculation in order to follow the evolution of cell encrustation (Fig. 8). In the first stage (30 min), a thin and discontinuous precipitation of Fe-phosphate started in the periplasm. In addition, colloidal Fe-rich particles could be observed at the surface of the cells. After 3 h, the periplasm was already completely encrusted. Globules located at the cell surface were widespread in 6-h old cultures and restricted to cells showing encrustation of the periplasm. After 3 days, a clear asymmetric mineral thickening was observed at the cell pole. Finally, globules at the cell surface were more numerous and thicker in 6-day old cultures. Superimposed to this general scheme, heterogeneities in the intensity of cell biomineralization were noticed among the bacterial populations. As shown in Fig. 9, cells devoid of any precipitate were observed in the cultures at each individual stage. These bacteria were observed by STEM (Fig. 9a) and were also clearly identified by STXM, appearing on C maps but not on Fe maps (Fig. 9b and c).

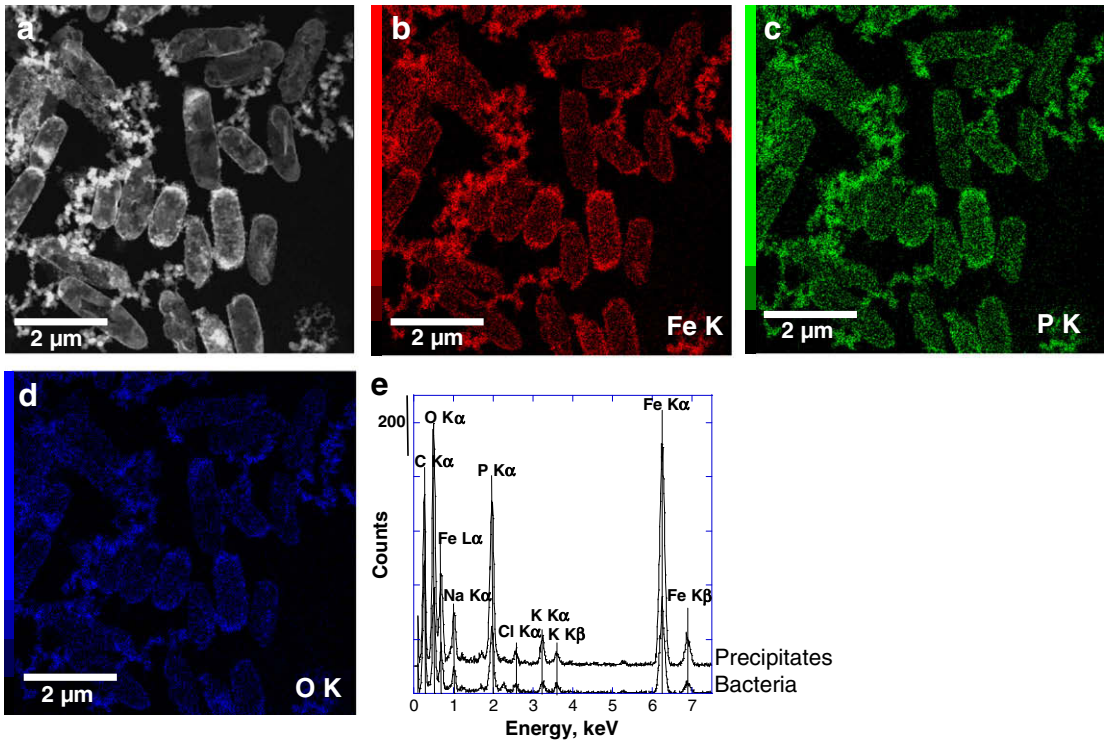

Fig. 6. Chemical composition of minerals formed in BoFeN1 culture after 6 days of culture. (a) STEM image (dark field) showing numerous cells of BoFeN1, most of which containing periplasmic iron-rich precipitates. (b, c and d) XEDS maps of Fe, P and O, respectively. (e) XEDS spectra measured on extracellular mineralized filaments and on bacteria.

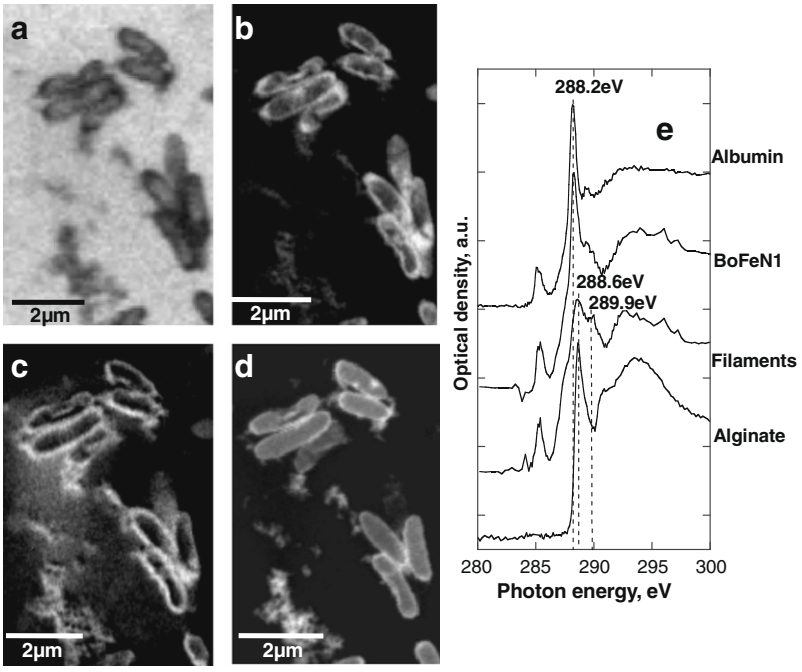

Fig. 7. Spectromicroscopy study of organics associated with BoFeN1 biominerals. (a) STXM image of BoFeN1 bacteria and precipitates at 288.2 eV. (b) Map of proteins obtained by subtracting the image at 280 eV converted into optical density units (OD) from the OD-image taken at 288.2 eV (maximum absorption of proteins). Bacteria cells can be easily detected on this map and show for some of them (e.g. left hand side) a higher protein concentration at the periphery and especially at the poles. (c) Map of carbon absorbing at 289.2 eV (maximum absorption of polysaccharides) showing the presence of exopolysaccharides in the vicinity of the cells. (d) Fe map obtained from the subtraction of the OD-image taken at 700 eV from the OD-image taken at 708.7 eV, showing a higher content of iron within the periplasm of the cells and the presence of extracellular iron-rich precipitates. (e) C K-edge NEXAFS spectra of the BoFeN1 bacteria, organics associated with the extracellular precipitates and of the reference compounds albumin (protein) and alginate (polysaccharide).

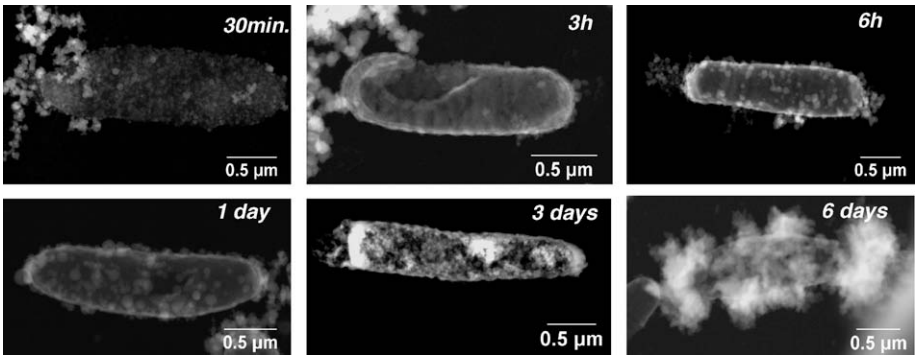

Fig. 8. Temporal evolution of BoFeN1 encrustation. STEM images (dark field) acquired 30 min to 6 days after inoculation showing the progressive encrustation of the periplasm, followed by the appearance of globules at the cell surface.

3.4. Evolution of iron redox state at the submicrometer scale in BoFeN1 cultures

The spatial distribution of iron redox states in BoFeN1 cultures was analyzed by STXM at the Fe $L_{2,3}$-edges (Fig. 10). Fe(II) and Fe(III) maps (Fig. 10a and b) were obtained by fitting Fe $L_{2,3}$-edges stacks with linear combinations of Fe $L_{2,3}$-edges spectra of the Fe(II)- and Fe(III)-phosphate model compounds and a constant (Fig. 10c). A color composite of the Fe(II) and Fe(III) maps (Fig. 10d) allowed the localization of oxidized versus reduced areas in the samples. The two references (Fe-phosphates) were also used for linear decomposition of the XANES spectra extracted from the stacks on bacteria and extracellular precipitates (Fig. 10e). Best fits provided a quantitative estimation of Fe(II)/Fe(total) and Fe(III)/Fe(total) ratios (Table 2) in the bacteria and in the extracellular precipitates. The optical density was systematically checked to ensure that it was low enough to avoid oversaturation of the absorption signal that could artifactually modify the Fe-redox ratio.

In 1-day old cultures, iron exhibited a mixed valence in bacteria as well as in extracellular precipitates, with average Fe(III)/Fe(total) ratios of $50 \pm 0.6\%$ and $44 \pm 0.6\%$ Fe(III), respectively (Fig. 10 and Table 2). Combining these results with the total Fe concentration (Fe(II) and Fe(III) in a dissolved or particulate form, 5.4 mM) and the dissolved Fe(II) concentration measured by spectrophotometry in the culture medium after 1 day of culture (3.6 mM), we can estimate particulate Fe(II) and Fe(III) average concentrations in the medium of 0.95 and 0.85 mM, respectively. However, spatial heterogeneities of the Fe redox state were detected within the extracellular precipitates (Fig. 10d): in particular, highly oxidized spots ($75 \pm 0.6\%$ Fe(III)) were observed among the extracellular precipitates.

Following the same method, the temporal evolution of iron redox state was investigated on samples collected 3 h to 6 days after inoculation. Fe(II)–Fe(III) composite maps (Fig. 11a–e) showed a progressive evolution from a predominantly Fe(II) composition on the cells and the extracellular precipitates (3–6 h) towards a completely oxidized, Fe(III) state in 6-day old samples. Accordingly, best fits of the XANES spectra of the bacteria (Fig. 11f and Table 2) evidenced a transition from a mixed valence Fe(II)–Fe(III) mineral ($42 \pm 0.5\%$ Fe(III)) towards an almost pure Fe(III) mineral ($91.7 \pm 0.7\%$ Fe(III)). The same trend was observed on the extracellular precipitates (Fig. 11g and

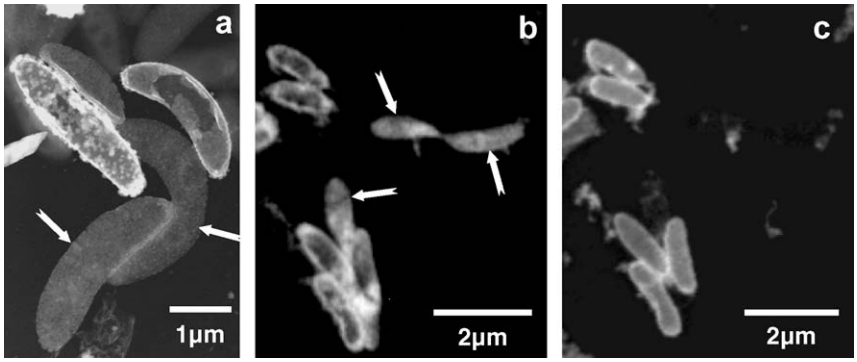

Fig. 9. Heterogeneity of encrustation among the bacterial population. (a) STEM image a BoFeN1 cells 6 days after inoculation, showing the coexistence of encrusted and non-encrusted bacteria (white arrows). (b) Map of proteins in a 1-day old culture obtained from the subtraction of the OD-image taken at 280 eV from the OD-image taken at 288.2 eV. White arrows point out non-encrusted cells. (c) Iron OD-map of the same area as (b) obtained from the subtraction of the OD-image taken at 700 eV from the OD-image taken at 708.7 eV. Non-encrusted cells are not visible on this map.

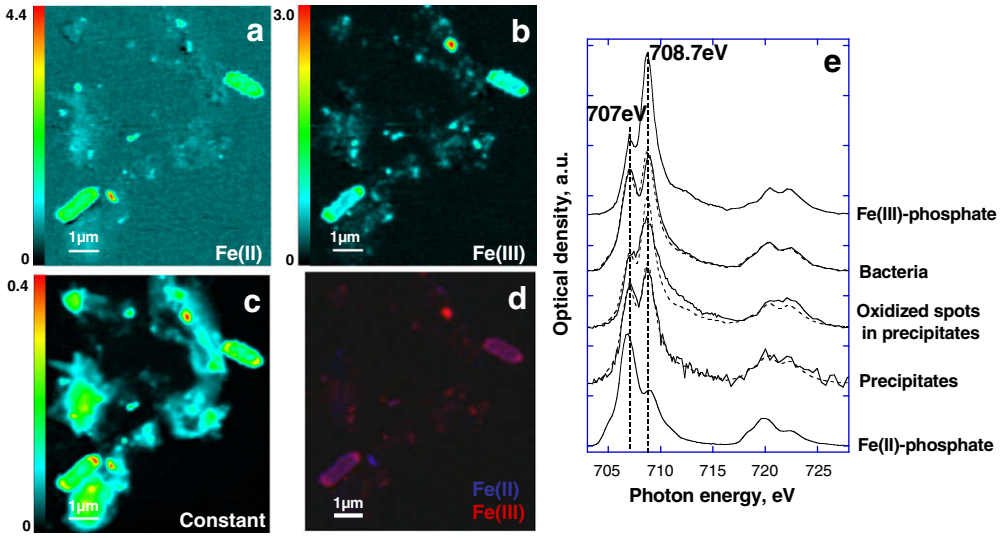

Fig. 10. Mapping of Fe(II) and Fe(III) in a 1-day old culture of BoFeN1. Stacks were fitted by a linear combination of a reference Fe(II)-phosphate, a reference Fe(III)-phosphate and a constant. (a and b) Fe(II) and Fe(III) maps obtained by fitting the stack with a reference Fe(II)-phosphate and a reference Fe(III)-phosphate, respectively. These maps show two encrusted cells and extracellular precipitates. (c) Constant map (i.e. contribution of a constant absorbance spectrum at each pixel) accounting for the absorption of all elements below the absorption edge energy of Fe. (d) Composite map obtained by overlaying the Fe(II)- and the Fe(III) maps of the same area (in blue and red, respectively), showing the presence of highly oxidized spots among the mixed-valence extracellular precipitates. (e) NEXAFS spectra at the Fe $L_{2,3}$-edge extracted from different areas of the stack compared with the spectra of Fe(II)-phosphate and Fe(III)-phosphate model compounds. Spectra (solid lines) were fit with combinations of the two model compounds to estimate the proportions of Fe(II) and Fe(III) (dashed lines). Numerical fit results are displayed in Table 2. (For interpretation of the references to color in this figure legend, the reader is referred to the web version of this paper.)

Table 2
Fe(III)/Fe(total) quantification obtained from the fit of Fe $L_{2,3}$-edge NEXAFS spectra extracted from stacks on bacteria and precipitates at different stages of the culture. Fe(III)/Fe(total) values result from at least two spectra fits. Standard deviations (SD) were calculated as the SD of the fit to the data. Values reported in this table are means of the standard deviations obtained for each fit.

Area	Time, h	Mean Fe(III)/Fe(total)	Standard deviation
Bacteria	3	0.42	0.005
	6	0.450	0.004
	24	0.50	0.006
	72	0.65	0.008
	144	0.917	0.007
Precipitates	3	0.37	0.006
	6	0.349	0.004
	24	0.44	0.006
	72	0.66	0.007

Table 2). These results parallel bulk measurements of dissolved Fe(II) in the cultures (Fig. 1).

4. DISCUSSION

4.1. Periplasmic and polar precipitation of iron phosphates

In the present study, we observed the precipitation of amorphous iron phosphates within the periplasm of the anaerobic iron-oxidizing nitrate-reducing strain BoFeN1 (Fig. 4). In contrast, in the anaerobic iron-oxidizing phototrophic purple bacteria strain SW2, the periplasm is never encrusted and precipitation of iron mainly occurs outside the cells (Kappler and Newman, 2004). The reason why these two strains, that both oxidize ferrous iron at neutral pH, exhibit different biomineralization patterns remains unclear. Precipitation of calcium and chromium phosphates within the periplasm has been reported in several other Gram-negative bacteria exposed to elevated concentrations calcium (Benzerara et al., 2004b) or chromate (Goulhen et al., 2006), respectively. This suggests that periplasmic mineralization of phosphates is a widespread mechanism, not restricted to iron-oxidizing bacteria. Moreover, the two latter studies proposed two separate processes to account for the preferential precipitation of phosphate in the periplasm: (1) the achievement of supersaturation with the phosphate phase within the periplasm and (2) the preferential nucleation of phosphate minerals on periplasmic, possibly protein, compounds. Regarding the achievement of supersaturation, it should be noted that the culture medium was initially saturated with a Fe(II)-phosphate phase (see medium preparation in Section 2). It is generally assumed that the chemical composition within the periplasm is close to that of the culture medium, given the high permeability of the outer membrane, due to the abundance of porins (Nikaido, 2003; Wilks and Slonczewski, 2007). Slight variations of chemical activities within the periplasm may locally increase supersaturation with a Fe-phosphate phase and account for its precipitation at this location. For exam-

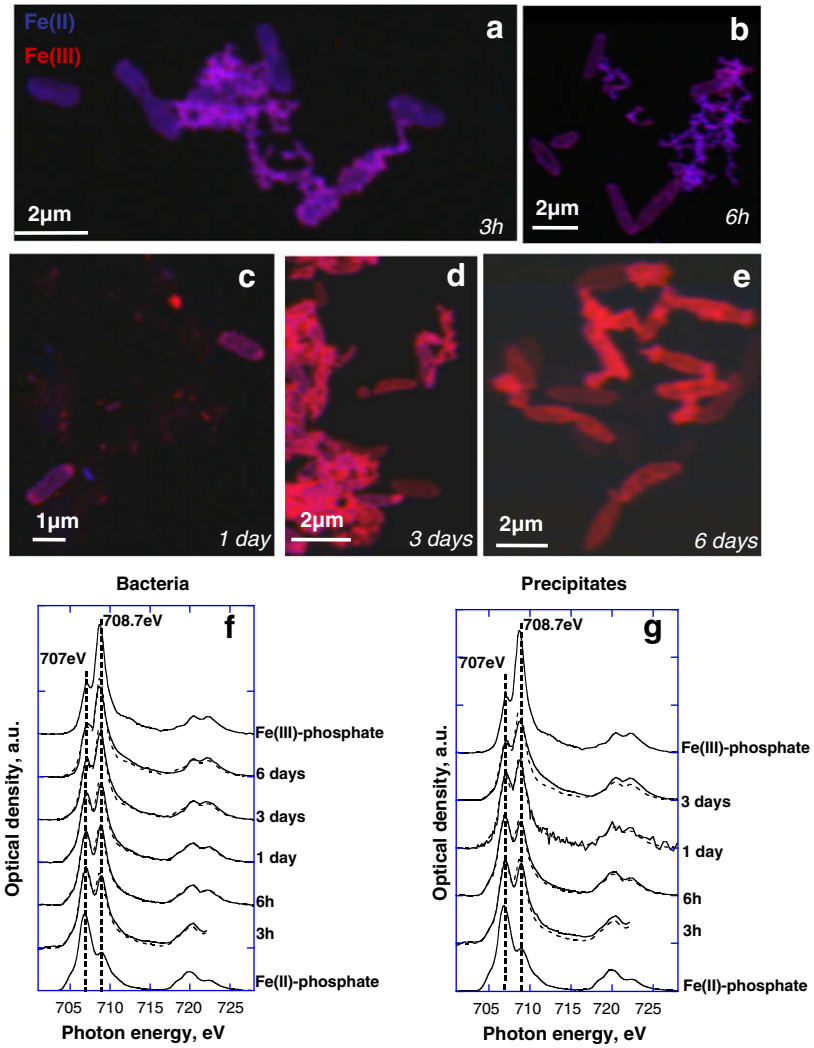

Fig. 11. Evolution of iron redox state 3 h to 6 days after inoculation. (a–e) Fe redox mapping (after the same procedure as presented in Fig. 10) after 3, 6, 24, 72 and 144 h of culture. We observed the progressive oxidation of iron associated with bacteria and extracellular precipitates. (f and g) NEXAFS spectra at the Fe $L_{2,3}$-edge obtained on bacteria and extracellular precipitates, respectively, collected on 3-h old to 6-days old cultures. Solid lines show the data and dashed lines the fits. The numerical results of the fits are displayed in Table 2. These results indicate the progressive oxidation of iron both at the contact of the bacteria and in the extracellular precipitates.

ple, these variations may be triggered by the recycling of phosphates involving the activity of phosphatases (e.g. Hirschler et al., 1990; Blake et al., 1998), by local variations of pH and/or by the metabolic oxidation of iron. The solubility of the amorphous Fe-phosphates detected in the present study is however unknown and thermodynamic analyses will have to be conducted in the future to address that point. Regarding a preferential nucleation of mineral phases within the periplasm, observations of a preferential crystallographic growth of apatite parallel to the cell surface and proteomics studies have suggested that formation of Ca-phosphate in the periplasm may result from nucleation on specific membrane-associated proteins (e.g. Van Dijk et al., 1998; Benzerara et al., 2004b). In BoFeN1 cultures, we observed an accumulation of proteins in the periplasm of iron-encrusted cells (Fig. 7). These periplasmic proteins could serve as nucleation sites for precipitation of iron phosphate, but further investigations are needed to support this hypothesis.

Proteins allocated to the periplasm are synthesized in the cytoplasm and translocated to the periplasmic compartment, where they are ultimately folded and assembled (Miot and Betton, 2004). It has been shown that various environmental stresses can enhance the accumulation of misfolded proteins in the periplasm of *Escherichia coli*, leading to the formation of periplasmic inclusion bodies composed of protein aggregates (e.g. Arié et al., 2006). Moreover, recent studies evidenced an asymmetric formation and accumulation of inclusion bodies at the poles of *E. coli*, under non-stressing conditions (Lindner et al., 2008). This asymmetric pattern was shown to be a direct consequence of aging: upon cell division, protein aggregates segregate and accumulate in older poles relative to new poles. In the present study, we observed both a periplasmic

accumulation of proteins in iron-encrusted cells and an asymmetric pattern of cell mineralization at the poles. These results are both suggestive of protein aggregation and the possible relation with a preferential cell encrustation would be interesting to study further. Alternatively, the preferential location of iron precipitates at the cell poles might be reminiscent of iron oxide granules previously reported to accumulate at the poles of the iron-reducing bacterium *Schewanella putrefaciens* (Glasauer et al., 2007). These authors proposed that this polar location could result from a facilitated iron uptake at the poles.

4.2. Evolution of iron redox state in the periplasm

Proteins involved in the transfer of electrons during iron oxidation by anaerobic nitrate-dependent iron-oxidizing bacteria are not known nor localized yet. However, recent studies of the anaerobic iron-oxidizing phototrophs *Rhodopseudomonas palustris* strain TIE-1 and *R. ferroxidans* strain SW2 suggested that a soluble decahaeme c-type cytochrome, potentially playing a crucial role in iron oxidation, could reside in the periplasm (Croal et al., 2007; Jiao and Newman, 2007). Similarly, in the acidophilic iron-oxidizing bacterium *Acidithiobacillus ferroxidans*, the electron transfer system coupled to iron oxidation is expected to function in the periplasmic space (Bruscella et al., 2005) and in particular, the cytochrome c oxidase has been described as a membrane-bound protein (Yamanaka and Fukomori, 1995). In the present study, significant amounts of Fe(III) within BoFeN1 periplasm were observed from the beginning of the culture, increasing over time. These results strongly suggest that at least one of the steps of iron oxidation takes place in the periplasm of this strain as well.

Given the high permeability of the outer membrane of Gram-negative bacteria, it is likely that the higher the Fe(II) concentration in the culture medium, the higher the Fe(II) concentration in the periplasm. Hypothesizing that Fe(II) oxidation occurs within the periplasm of BoFeN1, the redox state of periplasmic iron phosphates is directly influenced by the balance between soluble Fe(II) concentrations in the culture medium and Fe(III) formed by metabolic oxidation. The following scenario can thus be proposed: at time zero, there is a high concentration of Fe(II) in solution, and part of this iron is taken up and oxidized by the bacteria, leading to the precipitation of a mixed-valence iron phase in the periplasm. Over the course of culture growth, the concentration of dissolved Fe(II) in solution decreases and thus the average iron redox state of the periplasmic precipitate increases. This scenario could partly explain how the redox state of the periplasmic precipitate roughly follows the iron redox state of the bulk solution. Moreover, in a scenario where Fe oxidation stops as soon as precipitation occurs within the periplasm, one could expect to find a mixture of cells with periplasmic precipitates exhibiting various iron redox states ranging from a mixed-valence compound towards a pure Fe(III) compound in the latest stages of growth. In contrast, although the number of analyses was inherently limited by the microscopy approach, the iron redox state of the periplasmic precipitates was constant from one cell to another at a given growth stage. Two hypotheses could account for these results: (1) a constant re-equilibration of the redox state of the precipitates after their formation, or (2) an increasing fraction of biomineralizing cells at a given stage compared to former stages (potentially caused by a combination of growth and precipitation kinetics or by cell lysis). These hypotheses will have to be assessed in future studies. Overall, the homogeneity of the iron redox state and the colocalization of Fe and P evidenced by EDXS (Fig. 6) both suggest the existence of a single Fe-phosphate phase at a given stage of the culture. Some authors have proposed the existence of an autocatalytic process consisting in the oxidation of Fe(II) in solution by Fe(III)-containing solids. Fakih et al. (2008) have observed a decreased autocatalytic effect of the oxidation of Fe(II) associated with bacteria in cultures of *Bacillus subtilis*. While this process may occur in BoFeN1 cultures, it should be noted that it would slow down the rate of Fe(II) oxidation within the periplasm of BoFeN1 cells. However, the main trend we observe is the reverse, i.e. faster oxidation of Fe(II) on the cells, which likely results at first order from the metabolic oxidation of Fe(II) by the bacteria.

4.3. Extracellular precipitation of iron phosphates

4.3.1. Role of organics in extracellular precipitation of iron phosphates

Extracellular mineralized filaments consisting of iron phosphates were shown to be associated with exopolysaccharides (Fig. 7) in the BoFeN1 cultures. These precipitates displayed a morphology (Fig. 4) and an organic content similar to the polysaccharide-associated iron oxyhydroxide filaments described by Chan et al. (2004) in a neutral-pH environment. These authors suggested that extrusion of polysaccharides localized iron precipitation in proximity to the cell membranes, thus harnessing the proton gradient for energy generation. In addition, this study showed that polysaccharide strands triggered the nucleation of high aspect ratio pseudo-single crystals of akaganeite. In contrast, iron phosphates formed by BoFeN1 are amorphous. However, our results suggest that EPS may facilitate iron phosphate nucleation or aggregation of iron phosphate colloids outside the cells, concomitantly with periplasmic encrustation.

4.3.2. Origin of extracellular Fe(III)

STXM analyses of the extracellular precipitates formed in BoFeN1 cultures highlighted a local heterogeneity of iron redox state, with highly oxidized spots disseminated within a mixed-valence iron phosphate matrix (Fig. 10). Furthermore, iron was almost completely oxidized in the extracellular precipitates after three days of culture (Fig. 11 and Table 2). These extracellular iron biominerals are reminiscent of those described in neutrophilic iron-oxidizing phototroph cultures of *R. palustris* strain SW2 for instance (Kappler and Newman, 2004). Those authors have questioned the mechanisms involved in the transfer of Fe(III) from the cells to the extracellular medium. Indeed, the presence of Fe(III) away from the bacteria is somewhat surprising given the low solubility of Fe(III) at neutral pH

(Cornell and Schwertmann, 2003). The same question is relevant to BoFeN1, as we showed in the present study that BoFeN1, in addition to mineral precipitation within the periplasm and on external cell wall, has the ability to form extracellular Fe(III) mineral phases not bound to the cells. Abiotic oxidation of Fe(II) by nitrite can first be considered. However, such processes have been shown to contribute to a significant iron oxidation rate only in the presence of cell-bound Fe(II) and not in the presence of aqueous Fe(II) (Coby and Picardal, 2005). Moreover, as demonstrated by Kappler et al. (2005a), the kinetics of iron oxidation observed in BoFeN1 cultures does not support an abiotic oxidation of iron by nitrites. Therefore, abiotic oxidation of Fe(II) at distance from the cells via this mechanism is unlikely. Although significant amounts of proteins were not detected in association with extracellular precipitates, lysis of cells encrusted by Fe(III) minerals could account in part for the presence of Fe(III)-rich spots among the extracellular mixed-valence precipitates. Previous studies on *R. ferrooxidans* sp. strain SW2 (Croal et al., 2004; Kappler and Newman, 2004; Croal et al., 2007) have suggested some other mechanisms: (1) a production of Fe(III)-chelators exporting Fe(III) away from the cells (this hypothesis may also partly explain the Fe isotope fractionation produced by iron-oxidizing phototrophs (Croal et al., 2004)) (2) A local drop of pH around the cells (Kappler and Newman, 2004), which may favor Fe(III) export.

4.4. Potential bio-signatures in the fossil record

Mineralized filaments composed of iron oxides have been widely described in ancient rocks and their biogenicity questioned (e.g. Little et al., 2004; Ivarsson et al., 2008). Most of these studies have noted the morphological similarity of these filaments with structures resulting from iron oxidation by microaerobic bacteria such as *Gallionella* stalks and *Leptothrix* sheaths (Fortin and Langley, 2005). However, potential signatures of the past activity of anaerobic iron-oxidizing bacteria have never been observed in ancient rocks, probably as a consequence of the scarcity of studies dealing with these metabolisms. Nevertheless, anaerobic iron-oxidizing bacteria may have played a crucial role in driving ancient geochemical cycles (Konhauser, 1998; Kappler et al., 2005b; Posth et al., in press). Moreover, the potential involvement of iron-oxidizing bacteria in the formation of tubes in basaltic glass has been discussed (e.g. Furnes et al., 2005; Benzerara et al., 2007). In order to fully assess the biogenic origin of iron minerals found in ancient rocks and their possible relationship with the activity of past anaerobic iron-oxidizing bacteria, accurate and specific criteria are needed. In the present study, minerals produced in BoFeN1 cultures were shown to consist of Fe-phosphates. It is likely that using a different culture medium composition (for instance carbonate instead of phosphate) would have led to a different mineralogy. The mineralogy of the phases formed in the present BoFeN1 cultures is thus likely not innate to bacterial anaerobic Fe oxidation at neutral pH. This issue should be addressed in future experiments in which the chemistry of culture medium could be modified. Nevertheless, iron biominerals produced in BoFeN1 cultures were shown to exhibit very specific patters that are probably independent of the chemistry of the culture medium and more likely related to processes triggered by this bacterial metabolism: a 40-nm thick layer of iron minerals associated with high concentrations of protein moieties within the periplasm (Fig. 4), asymmetric mineralization at bacteria poles (Fig. 4), and mineralized filaments composed of iron minerals associated with polysaccharides (Figs. 4 and 7). These features are potential indicators of these metabolisms that could be preserved and sought for in modern environments and in ancient rocks. The preservation of such features during diagenesis and metamorphism, in particular the preservation of local accumulations of proteins and polysaccharides associated with the mineral precipitates will have to be assessed in future experiments. Looking for such organic–mineral associations using spectromicroscopic methods (e.g. Bernard et al., 2007; Lepot et al., 2008) would provide additional evidence of bacterial iron oxidation in the fossil record.

5. CONCLUSIONS

The periplasm was revealed as a key location for iron oxidation in BoFeN1. Asymmetric polar mineral thickening and accumulation of proteins within the periplasm of iron-encrusted cells are suggestive of protein aggregation possibly promoting iron phosphate nucleation. Exopolysaccharides were produced and released by the bacteria and potentially participate in localizing the precipitation of extracellular iron phosphates at distance from the cells. The progressive oxidation of these extracellular phases supports the hypothesis of a mechanism of Fe(III) export. These results indicate that this encrusting strain (BoFeN1) shares similarities with non-encrusting neutrophilic iron-oxidizing bacteria, such as SW2 (Kappler and Newman, 2004), suggesting that cell encrustation is not exclusive of Fe(III) export.

ACKNOWLEDGMENTS

We gratefully acknowledge the support of an ANR "Jeunes Chercheurs" Grant (J.M. and K.B.).

The STXM measurements have been performed at the Swiss Light Source, Paul Scherrer Institut, Villigen, Switzerland and the Canadian Light Source, Saskatoon, Canada. The CLS is supported by NSERC, CIHR, NRC and the University of Saskatchewan. We thank Joerg Raabe and George Tzvetkov for their expert support of the SLS STXM and Konstantine Kaznatcheev, Chithra Karunakaran and Drew Bertwistle for their expert support of the CLS STXM. We also thank Olivier Beyssac (ENS Paris) for his help in data collection at SLS. Portions of this research were carried out at the Stanford Synchrotron Radiation Laboratory, a national user facility operated by Stanford University on behalf of the US Department of Energy, Office of Basic Energy Sciences. The authors are indebted to the SSRL staff, especially John R. Bargar, Joe Rogers and Samuel Webb, for their technical assistance during the XAFS experiments. We also thank Georges Ona N'guema and Farid Juillot (IMPMC) for their help in XAS data collection at the SSRL. We acknowledge the European Synchrotron Radiation Facility for provision of synchrotron radiation facilities and we thank Olivier Mathon for his assistance in using beamline BM29. We acknowledge the SOLEIL Synchrotron for provision of syn-

chrotron radiation facilities and we thank Stephanie Belin, Emiliano Fonda and Valerie Briois for their assistance in using the SAMBA beamline. We acknowledge Florian Hegler for his help cultivating the nitrate-depending Fe(II)-oxidizing strain BoFeN1. The contribution from AK and NP was funded by an Emmy-Noether fellowship and additional funding from the German Research Foundation (DFG) to AK. This study was supported by a grant from Agence Nationale de la Recherche (K.B. and J.M.). This is IPGP contribution No. 2441. This work was supported by ACI/FNS grant 3033.

APPENDIX A. SUPPLEMENTARY DATA

Supplementary data associated with this article can be found, in the online version, at doi:10.1016/j.gca.2008.10.033.

REFERENCES

Ankudinov A. L., Ravel B., Rehr J. J. and Conradson S. D. (1998) Real-space multiple-scattering calculation and interpretation of X-ray-absorption near-edge structure. *Phys. Rev. B (Condens. Matter)* **58**, 7565–7576.

Arié J. P., Miot M., Sassoon N. and Betton J. M. (2006) Formation of active inclusion bodies in the periplasm of *Escherichia coli*. *Mol. Microbiol.* **62**(2), 427–437.

Benz M., Brune A. and Schink B. (1998) Anaerobic and aerobic oxidation of ferrous iron at neutral pH by chemoheterotrophic nitrate-reducing bacteria. *Arch. Microbiol.* **169**, 159–165.

Benzerara K., Yoon T.-H., Tyliszczak T., Constantz B., Spormann A. M. and Brown, Jr., G. E. (2004a) Scanning transmission X-ray microscopy study of microbial calcification. *Geobiology* **2**, 249–259.

Benzerara K., Menguy N., Guyot F., Skouri F., de Luca G., Barakat M. and Heulin T. (2004b) Biologically controlled precipitation of calcium phosphate by *Ramlibacter tataouinensis*. *Earth Planet. Sci. Lett.* **228**, 439–449.

Benzerara K., Menguy N., Banerjee N. R., Tyliszczak T., Guyot F. and Brown, Jr., G. E. (2007) Alteration of submarine basaltic glass from the Ontong Java Plateau: a STXM and TEM study. *Earth Planet. Sci. Lett.* **260**, 187–200.

Bernard S., Benzerara K., Beyssac O., Menguy N., Guyot F., Brown G. E. and Goffé B. (2007) Exceptional preservation of fossil plant spores in high-pressure metamorphic rocks. *Earth Planet. Sci. Lett.* **262**, 257–272.

Blake R. E., O'Neil J. R. and Garcia G. A. (1998) Effects of microbial activity on the delta O-18 of dissolved inorganic phosphate and textural features of synthetic apatites. *Am. Mineral.* **83**, 1516–1531.

Bruscella P., Cassagnaud L., Ratouchniak J., Brasseur G., Lojou E., Amils R. and Bonnefoy V. (2005) The HiPIP from the acidophilic *Acidithiobacillus ferroxidans* is correctly processed and translocated in *Escherichia coli*, in spite of the periplasm pH difference between these two micro-organisms. *Microbiol. SGM* **151**, 1421–1431.

Chan C. S., De Stasio G., Welch S. A., Girasole M., Frazer B. H., Nesterova M. V., Fakra S. and Banfield J. F. (2004) Microbial polysaccharides template assembly of nanocrystal fibers. *Science* **303**, 1656–1658.

Clarke W. A., Konhauser K. O., Thomas J. C. and Bottrell S. H. (1997) Ferrix hydroxide and ferric hydroxysulfate precipitation by bacteria in an acid mine drainage lagoon. *FEMS Microbiol. Rev.* **20**, 351–361.

Coby A. J. and Picardal F. W. (2005) Inhibition of NO_3^- and NO_2^- reduction by microbial Fe(III) reduction: evidence of a reaction between NO_2^- and cell surface-bound Fe^{2+}. *Appl. Environ. Microbiol.* **71**, 5267–5274.

Cornell R. M. and Schwertmann U. (2003) *The Iron Oxides: Structure, Properties, Reactions Occurrences and Uses*. Wiley-VCH Verlag GmbH & Co, Weinheim, Germany.

Croal L. R., Johnson C. M., Beard B. L. and Newman D. K. (2004) Iron isotope fractionation by Fe(II)-oxidizing photoautotrophic bacteria. *Geochim. Cosmochim. Acta* **68**, 1227–1242.

Croal L. R., Jiao Y. and Newman D. K. (2007) The fox operon from *Rhodobacter* strain SW2 promotes phototrophic Fe(II) oxidation in *Rhodobacter capsulatus* SB1003. *J. Bacteriol.* **189**, 1774–1782.

Ehrenreich A. and Widdel F. (1994) Anaerobic oxidation of ferrous iron by purple bacteria, a new-type of phototrophic metabolism. *Appl. Environ. Microbiol.* **60**, 4517–4526.

Fakih M., Châtellier X., Davranche M. and Dia A. (2008) *Bacillus subtilis:* Bacteria hinder the oxidation and hydrolysis of Fe^{2+} ions. *Environ. Sci. Technol.* **42**, 3194–3200.

Fejdi P., Poullen J. F. and Gasperin M. (1980) Refinement of the structure of vivianite, $Fe_3(PO_4)_2{\cdot}8H_2O$. *Bull. Miner.* **103**, 135–138.

Forsyth J. B., Hedley I. G. and Johnson C. E. (1968) Magnetic structure and hyperfine field of goethite (alpha-FeOOH). *J. Phys. C (Solid State Phys.)* **1**, 179–188.

Fortin D. and Langley S. (2005) Formation and occurrence of biogenic iron-rich minerals. *Earth Sci. Rev.* **72**, 1–19.

Furnes H., Banerjee N. R., Muehlenbachs K. and Kontinen A. (2005) Preservation of biosignatures in metaglassy volcanic rocks from the Jormua ophiolite complex, Finland. *Precambrian Res.* **136**, 125–137.

Ghiorse W. C. (1984) Biology of iron-depositing and manganese-depositing bacteria. *Ann. Rev. Microbiol.* **38**, 515–550.

Glasauer S., Langley S., Boyanov M., Lai B., Kemner K. and Beveridge T. J. (2007) Mixed-valence cytoplasmic iron granules are linked to anaerobic respiration. *Appl. Environ. Microbiol.* **73**, 993–996.

Goulhen F., Gloter A., Guyot F. and Bruschi M. (2006) Cr(VI) detoxification by *Desulfovibrio vulgaris* strain Hildenborough: microbe–metal interactions studies. *Appl. Microbiol. Biotechnol.* **71**, 892–897.

Hafenbradl D., Keller M., Dirmeier R., Rachel R., Rossnagel P., Burggraf S., Huber H. and Stetter K. O. (1996) Ferroglobus placidus gen nov, sp nov, a novel hyperthermophilic archeum that oxidizes Fe2+ at neutral pH under anoxic conditions. *Arch. Microbiol.* **166**, 308–314.

Hallberg R. and Ferris F. G. (2004) Biomineralization by *Gallionella*. *Geomicrobiol. J.* **21**, 325–330.

Heising S. and Schink B. (1998) Phototrophic oxidation of ferrous iron by a *Rhodomicrobium vannielii* strain. *Microbiology* **144**, 2263–2269.

Hirschler A., Lucas J. and Hubert J. C. (1990) Apatite genesis, a biologically induced or biologically controlled mineral formation process. *Geomicrobiol. J.* **8**, 47–56.

Hitchcock A. P. (2001) Soft X-ray spectromicroscopy of polymers and biopolymer interfaces. *J. Synchrotron Radiat.* **8**, 66–71.

Ivarsson M., Lindblom S., Broman C. and Holm N. G. (2008) Fossilized microorganisms associated with zeolite–carbonate interfaces in sub-seafloor hydrothermal environments. *Geobiology* **6**, 155–170.

Jiao Y. and Newman D. K. (2007) The *pio* operon is essential for phototrophic Fe(II) oxidation in *Rhodopseudomonas palustris* TIE-1. *J. Bacteriol.* **189**, 1765–1773.

Kappler A. and Newman D. K. (2004) Formation of Fe(III)-minerals by Fe(II)-oxidizing phototrophic bacteria. *Geochim. Cosmochim. Acta* **68**, 1217–1226.

Kappler A. and Straub K. L. (2005) Geomicrobiological cycling of iron. *Mol. Geomicrobiol. Rev. Mineral. Geochem.* **59**, 85–108.

Kappler A., Schink B. and Newman D. K. (2005a) Fe(III) mineral formation and cell encrustation by the nitrate-dependent Fe(II)-oxidizer strain BoFeN1. *Geobiology* **3**, 235–245.

Kappler A., Pasquero C., Konhauser K. O. and Newman D. K. (2005b) Deposition of banded iron formations by photoautotrophic Fe(II)-oxidizing bacteria. *Geology* **33**, 865–868.

Kaznatcheev K. V. (2007) Soft X-ray spectromicroscopy beamline at the CLS: commissioning results. *Nucl. Instrum. Methods Phys. Res. A Accelerators Spectrometers Detectors Assoc. Equipment* **582**, 96–99.

Konhauser K. O. (1998) Diversity of bacterial iron mineralization. *Earth Sci. Rev.* **43**, 91–121.

Kozubal M., Macur R. E., Korf S., Taylor W. P., Ackerman G. G., Nagy A. and Inskeep W. P. (2008) Isolation and distribution of a novel iron-oxidizing crenarchaeon from acidic geothermal springs in Yellowstone National Park. *Appl. Environ. Microbiol.* **74**, 942–949.

Lazaroff N., Melanson L., Lewis E., Santoro N. and Pueschel C. (1985) Scanning electron-microscopy and infrared-spectroscopy of iron sediments formed by *Thiobacillus ferroxidans*. *Geomicrobiol. J.* **4**, 231–268.

Lepot K., Benzerara K., Brown, Jr., G. E. and Philippot P. (2008) Nanoscale evidence for microbial mineralization of Archean stromatolites. *Nat. Geosci.* **1**, 118–121.

Lindner A. B., Madden R., Demarez A., Stewart E. J. and Taddei F. (2008) Asymmetric segregation of protein aggregates is associated with cellular aging and rejuvenation. *PNAS* **105**, 3076–3081.

Little C. T. S., Glynn S. E. J. and Mills R. A. (2004) Four-hundred-and-ninety-million-year record of bacteriogenic iron oxide precipitation at sea-floor hydrothermal vents. *Geomicrobiol. J.* **21**, 415–429.

Michel F. M., Ehm L., Antao S. M., Lee P. L., Chupas P. J., Liu G., Strongin D. R., Schoonen M. A. A., Phillips B. L. and Parise J. B. (2007) The structure of ferrihydrite, a nanocrystalline material. *Science* **316**, 1726–1729.

Miot M. and Betton J. M. (2004) Protein quality control in the bacterial periplasm. *Microb. Cell Factories* **3**, doi:10.1186/1475.2859.3.4.

Morin G., Ona-Nguema G., Wang Y., Menguy N., Juillot F., Proux O., Guyot F., Calas G. and Brown, Jr., G. E. (2008) Extended X-ray absorption fine structure analysis of arsenite and arsenate adsorption on maghemite. *Environ. Sci. Technol.* **42**, 2361–2366.

Nikaido H. (2003) Molecular basis of bacterial outer membrane permeability revisited. *Microbiol. Mol. Biol. Rev.* **67**, 593.

Paktunc D., Dutrizac J. and Gertsman V. (2008) Synthesis and phase transformations involving scorodite, ferric arsenate and arsenical ferrihydrite: implications for arsenic mobility. *Geochim. Cosmochim. Acta* **72**, 2649–2672.

Posth N. R., Konhauser K. O. and Kappler A. (2008) Microbiological processes in BIF deposition. *Nat. Geosci.* **1**, 703–708.

Pratesi G., Cipriani C., Giuli G. and Birch W. D. (2003) Santabarbaraite: a new amorphous phosphate mineral. *Eur. J. Mineral.* **15**, 185–192.

Rose J., Manceau A., Bottero J. Y., Masion A. and Garcia F. (1996) Nucleation and growth mechanism of Fe oxyhydroxide in the presence of PO4 ions. 1. Fe K-edge EXAFS study. *Langmuir* **12**, 6701–6707.

Rose J., Flank AM., Masion A., Bottero JY. and Elmerich P. (1997) Nucleation and growth mechanisms of Fe oxyhydroxide in the presence of PO4 ions. 2. P K-edge EXAFS study. *Langmuir* **13**, 1827–1834.

Schwertmann U. and Cornell R. M. (1991) *Iron Oxides in the Laboratory: Preparation and Characterization*. VCH Publishers, Germany.

Straub K. L., Benz M., Schink B. and Widdel F. (1996) Anaerobic, nitrate-dependent microbial oxidation of ferrous iron. *Appl. Environ. Microbiol.* **62**, 1458–1460.

Straub K. L. and Buchholz-Cleven B. E. E. (1998) Enumeration and detection of anaerobic ferrous iron-oxidizing, nitrate-reducing bacteria from diverse European sediments. *Appl. Environ. Microbiol.* **64**, 4846–4856.

Thole B. T., Van der Laan G. and Fabrizio M. (1994) Magnetic ground state properties and spectral distributions I. X-ray absorption spectra. *Phys. Rev. B* **50**, 11466–11473.

Van Dijk S., Dean D. D., Liu Y., Zhao Y., Chirgwin J. M., Schwartz Z. and Boyan B. D. (1998) Purification, amino acid sequence and cDNA sequence of a novel calcium-precipitating proteolipid involved in calcification of *Corynebacterium matruchotii*. *Calcif. Tissue Int.* **62**, 350–358.

Viollier E., Inglett P. W., Hunter K., Roychoudhury A. N. and Van Cappellen P. (2000) The ferrozine method revisited: Fe(II)/Fe(III) determination in natural waters. *Appl. Geochem.* **15**, 785–790.

Webb S. (2004) SIXPACK: a graphical user interface for XAS analysis using IFEFFIT. *Phys. Scripta* **T115**, 1011–1014.

Weber K. A., Achenbach L. A. and Coates J. D. (2006) Microorganisms pumping iron: anaerobic microbial iron oxidation and reduction. *Nature* **4**, 752–764.

Widdel F., Schnell S., Heising S., Ehrenreich A., Assmus B. and Schink B. (1993) Ferrous iron oxidation by anoxygenic phototrophic bacteria. *Nature* **362**, 834–836.

Wilke M., Farges F., Petit P. E., Brown, Jr., G. E. and Martin F. (2001) Oxidation state and coordination of Fe in minerals: an Fe K-XANES spectroscopic study. *Am. Mineral.* **86**, 714–730.

Wilks J. C. and Slonczewski J. L. (2007) PH of the cytoplasm and periplasm of *Escherichia coli*: rapid measurement by green fluorescent protein fluorimetry. *J. Bacteriol.* **189**, 5601–5607.

Winterer M. (1997) XAFS – a data analysis program for material science. *J. Phys. IV* **7**, 243–244.

Yamanaka T. and Fukomori Y. (1995) Molecular aspects of the electron transfer system which participates in the oxidation of ferrous iron by *Thiobacillus ferroxidans*. *FEMS Microbiol. Rev.* **17**, 401–413.

Associate editor: Liane G. Benning